www.acsnano.org

Kinetic Control for Continuously Tunable Lattice Parameters, Size, and Composition during CsPbX₃ (X = Cl, Br, I) Nanorod Synthesis

Je-Ruei Wen, Freddy Alberto Rodríguez Ortiz, Anna Champ, and Matthew T. Sheldon*



Downloaded via TEXAS A&M UNIV COLG STATION on July 27, 2022 at 13:38:01 (UTC). See https://pubs.acs.org/sharingguidelines for options on how to legitimately share published articles.

Cite This: ACS Nano 2022, 16, 8318-8328



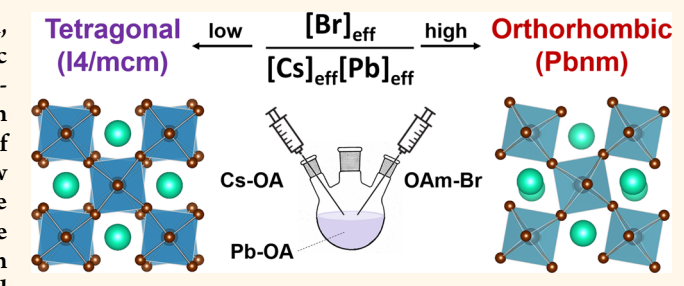
ACCESS

Metrics & More

Article Recommendations

Supporting Information

ABSTRACT: The fast kinetics of all-inorganic CsPb X_3 (X = Cl, Br, or I) nanocrystal growth entail that many synthetic strategies for structural control established in other semiconductor systems do not apply. Rather, products are often determined by thermodynamic factors, limiting the range of synthetic outcomes and functionality. In this study, we show how reaction kinetics are significantly slowed if nanocrystals are prepared using a dual injection strategy that moderates the crucial interaction between cesium and halide during nucleation and growth. The result is highly uniform nanorod or cuboid



nanocrystals with a controllable size and aspect ratio across the quantum confinement regime, obtainable for both pure and mixed halide compositions. Further, the crystal lattice is continuously tunable between the tetragonal (I4/mcm) and orthorhombic (Pbnm) phases, independent of the overall nanorod morphology, enabling significantly more sophisticated structure—property relationships that can be tailored during this kinetically controlled synthesis.

KEYWORDS: cesium lead halide, nanorods, slow injection, kinetic control, crystal phase control, tetragonal

ll-inorganic lead halide perovskite (LHP) nanocrystals (NCs) with the composition CsPb X_3 (X = Cl, Br, or I) have been studied extensively over the last several years for applications in photovoltaic cells, light-emitting diodes, photodetectors, and related technologies owing to their excellent optical and electronic properties such as tunable emission wavelengths, high photoluminescence quantum yield (PLQY), large oscillator strength, and large diffusion lengths. In common with other semiconductor systems, the nanocrystal properties are highly dependent on size, shape, and crystal phase. For optoelectronic applications, anisotropic morphologies such as one-dimensional nanorods are of particular interest due to their polarized light emission and opportunities for enhanced photogenerated charge separation, especially if quantum confinement of the excitonic transition can be maintained.2

Recent approaches for preparing $CsPbX_3$ nanorods include polar solvent-assisted growth, aging of preformed clusters, self-digestion or chemical cutting of larger $CsPbX_3$ nanowires, cation exchange on Cs_2MBr_4 (M=Zn, Hg, Cd) nanorods, conversion of Cs_4PbBr_6 NCs at water interfaces, these strategies generally result in nanorod diameters larger than the scale of significant quantum confinement, with little or no control over the aspect ratio. Rather, the range of

what can be achieved has been limited by intrinsic synthetic challenges associated with the materials system, as described in more detail below. Furthermore, the progression of 1-D nanostructures in a direct synthesis has never been observed; thus, the growth direction as well as the growth dynamics have remained unclear.¹⁷

Compared to the interest in shape and size, there has been significantly less development of synthetic strategies that control the crystal phase. In general, the crystal phase can be categorized as cubic, tetragonal, or orthorhombic. ¹⁸ For CsPbBr₃, cubic and orthorhombic phases are commonly observed, whereas there are only a few reports of tetragonal structures, varying with symmetry corresponding to *I4/mcm*, *P4/mbm*, or *P4₂mc*. The tetragonal *I4/mcm* structure has been observed in a single crystal sample ¹⁹ and has been detected indirectly in a nanocrystal thin film over a temperature range of 7–360 K. ²⁰ In contrast, the *P4/mbm* and *P4₂mc* structures

Received: March 11, 2022 Accepted: May 9, 2022 Published: May 11, 2022





result from thermal or optical stimulation, respectively. Additionally, the cubic, tetragonal, and orthorhombic phases can coexist, supporting well-defined stoichiometric interfaces even within individual nanoparticles. 20,24 While LHPs appear to maintain relatively similar band-edge transition energies and high PLQY across these crystal phases, 25 other properties such as the electron–phonon coupling strength and the efficiency for polaron formation depend strongly on details of the lattice structure, especially the tilt angle and deformation of the $[PbX_6]^{4-}$ octahedron units in these different phases. 26,27

A primary limitation to more sophisticated control of the crystal shape or phase—and a challenge for further optimization of the CsPbX3 system more generally—is the extremely fast reaction kinetics, with crystal growth completed in seconds after precursor injection in most synthetic protocols. 28,29 Thus, a lack of time separation between crystal nucleation and growth entails that the reaction system cannot easily be driven away from the thermodynamically preferred nanocrystal product.30 This is problematic, because decades of insight into nanocrystal synthesis have established that controlling reaction kinetics is crucial for the preparation of sophisticated morphologies and compositions that may not be attainable via shifting the thermodynamic equilibrium. 31,32 Under optimized kinetic conditions, the rate of atom deposition relative to that of surface diffusion can be modified, bringing about different crystal evolution mechanisms.³¹ When the surface diffusion rate is relatively higher, there is sufficient time for adatoms to move across nanocrystal surfaces, leading to the exposure of more thermodynamically stable facets. If the relative rate of deposition is greater, on the contrary, the adatoms are accumulated at the active sites, presenting facets with a higher surface energy as well as the possibility of kinetically trapped local bonding arrangements or distinct overall nanocrystal morphology.

With this limitation in mind, our previous study probed the growth kinetics of CsPbX₃ NCs and established that the reaction rate can be greatly reduced by controlling the availability of halide.³³ In the case of CsPbBr₃ NCs, with the slow introduction of Br ions, Cs ions first combine with Br ions to form CsBr NCs. Over several minutes, the CsBr seeds undergo a series of phase transformations from CsBr to Cs₄PbBr₆ followed by conversion into the commonly observed cuboid CsPbBr₃ NCs. Interestingly, this evolution is largely insensitive to the concentration of Pb ions.

In this report, we show how the relative rates of atom deposition and migration during crystal growth can be controlled with an even higher precision using a synthetic protocol based on the slow, simultaneous release of separate halide and Cs precursors into a Pb precursor solution. This procedure moderates the crucial interaction between Cs and halide during crystal nucleation and growth, providing crystallization into one-dimensional nanorods that extend in length with reaction time. By adjusting the reaction variables, the overall size and aspect ratio of nanorods can be modified across a size regime with strong quantum confinement. Further, the crystal phase is continuously tunable between tetragonal (I4/mcm) and orthorhombic structures, independent of the overall nanorod morphology, underlying that the lattice structure is a kinetically trapped, metastable product based on the external reaction conditions. Thus, we report an unambiguous example of a colloidal LHP synthesis with systematic control over a kinetically defined nanocrystal product in the quantum-confined regime.

RESULTS AND DISCUSSION

Synthesis of CsPbBr₃ Nanorods. In a typical synthesis, cesium oleate and oleylammonium bromide were prepared as separate precursor solutions mixed with oleic acid (OA) and oleylamine (OAm) in 1-octadecene (ODE) or toluene. Both precursors were simultaneously injected over the course of 5 min or longer into a lead oleate solution kept at 80 °C (Figure 1a, see the Methods section for details). The product was

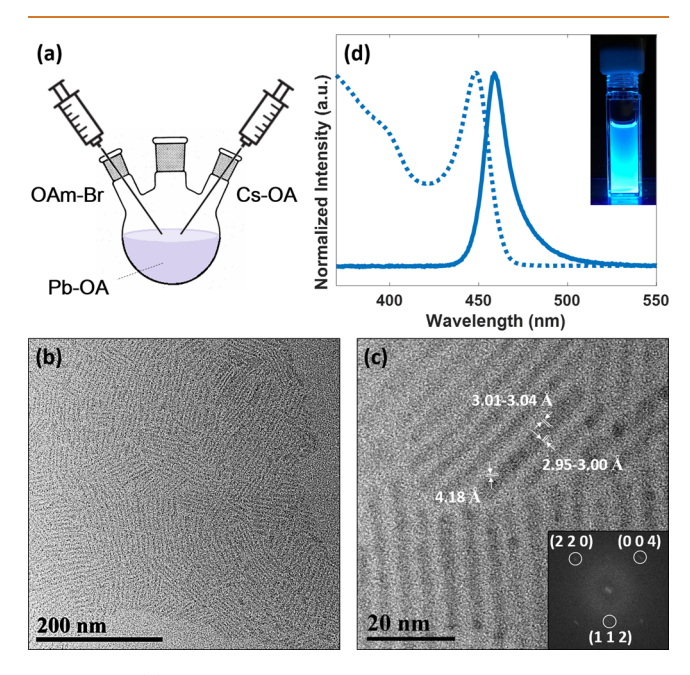


Figure 1. (a) Schematic illustration of a dual slow injection synthesis. (b and c) HRTEM images and (d) UV-vis spectra of CsPbBr₃ nanorods. In (c), the FFT of a nanorod is provided in the inset. In (d), the absorption and PL spectra are illustrated in dashed and solid curves, respectively. A photograph of the sample illuminated by a UV lamp is provided in the inset.

isolated by centrifugation and redispersed in hexane. Highresolution transmission electron microscopy (HRTEM) images of a representative sample are shown in Figure 1b,c. The nanocrystals exhibit a one-dimensional nanorod morphology with an average length and width of 39.32 \pm 10.34 and 3.88 ± 0.57 nm, respectively. Isolated nanorods were not identified unless TEM grids were prepared under highly diluted conditions (Figure S1). This well-organized, side-byside stacking appears to be common for 1-D CsPbBr₃, ^{9,11} in contrast with other 1-D semiconductor nanorods, such as CdSe/CdS or PbS, even with similar ligand shells. Lattice spacings around 3.01-3.05, 2.95-3.00, and 4.18-4.24 Å are identified along the long, short, and diagonal axes. This lattice spacing is obviously larger than the 2.9 and 4.1 Å fringes generally observed from cuboid CsPbBr3 NCs. In Figure 1c, some higher contrast dots are also observed, corresponding to metallic lead particles introduced by e-beam damage. This unavoidable beam damage, sometimes called lead leakage, is commonly observed across LHP systems.³⁴

In Figure 1d, the absorption spectrum shows a sharp absorption edge and a well-defined first excitonic absorption peak, suggesting strong quantum confinement and a narrow size distribution. Interestingly, the photoluminescence (PL) spectrum displays asymmetric broadening on the low energy side. Such PL broadening has been commonly observed

in strongly quantum-confined $CsPbBr_3$ nanorods, nanowires, and nanoplatelets, $^{9,11,37-39}$ and the broadening is typically attributed to size polydispersity or localized state emission (LSE). Here, the PL broadening is very likely associated with LSE, on the basis of the well-defined absorption features, the apparent sample uniformity by TEM, and photoluminescence excitation (PLE) studies of the nanorods and corresponding intermediates (see Figure S2 and discussion in the SI).

The crystal structure was examined using powder X-ray diffraction (XRD) (Figure 2a,b). In the low-angle region (2θ <

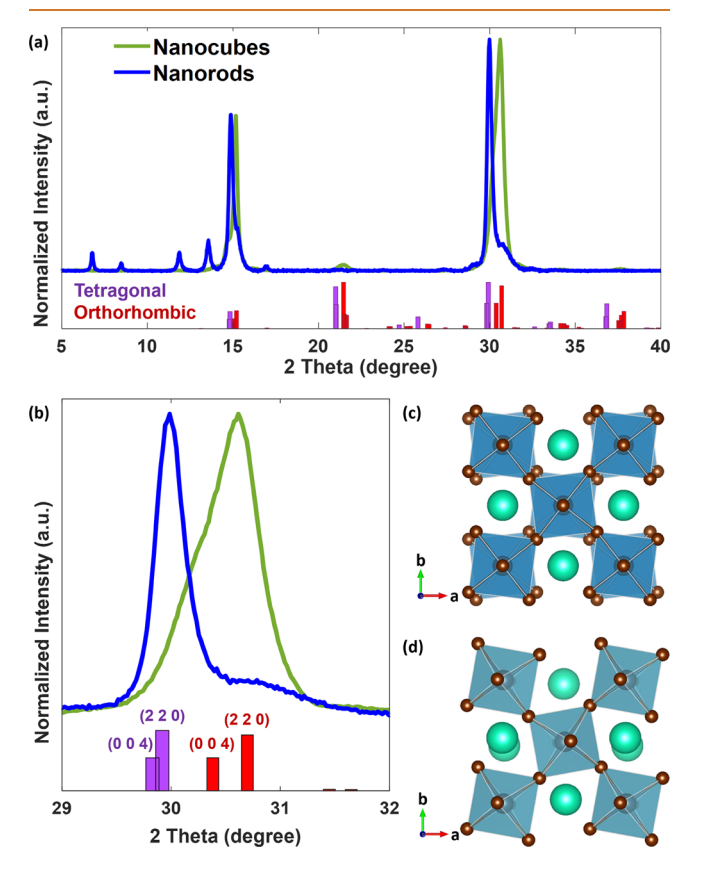


Figure 2. (a and b) XRD pattern of CsPbBr₃ nanorods (blue trace). Schematic crystal structures of (c) tetragonal (*I*4/*mcm*) and (d) orthorhombic (*Pbnm*) CsPbBr₃. In (a and b), card files for orthorhombic *Pbnm* (COD 1533062) and tetragonal *I*4/*mcm* (mp-1014168) as well as the diffractogram of conventional CsPbBr₃ nanocubes (green trace) are included for comparison.

15°), the peak spacing indicates a mesoscale periodicity of ca. 9.2 nm, consistent with the regular pitch of 7.8–9.2 nm between nanorods as revealed in the HRTEM images. At a higher scattering angle, surprisingly, the sample does not show the common orthorhombic or cubic crystal phase signatures of cuboid CsPbBr₃ NCs. Rather, the diffractogram indicates the nanorods adopt a tetragonal phase with *I4/mcm* symmetry (Figure 2c). The corresponding *d*-spacing values of the tetragonal phase match well with the lattice fringes observed in Figure 1c, with the fringes around 4.2 Å assigned to the (1 1 2) plane. Unfortunately, the difference between the (0 0 4) and (2 2 0) planes is less than 0.01 Å, so that an unambiguous assignment is not possible. Nonetheless, the fringes along the long axis appear to have slightly larger spacing than those along the short axis, suggesting the nanorods were grown along the

<0 0 2> direction with the $\{1\ 1\ 0\}$ surfaces being the exposed facets. If so, this growth would be consistent with conventional orthorhombic CsPbBr₃ crystals for which the $\{1\ 1\ 0\}$ facets have the lowest surface energy and are thus the primary exposed surfaces. 42,43

Thermodynamic Insights into 1-D Growth. The key experimental protocol that promotes one-dimensional nanorod growth is the slow, simultaneous injection of the separate precursor solutions. We hypothesize that slowing the release of Cs and Br modulates the rate at which atoms accumulate on growing nanocrystal seeds. With the slow injection, the adatom surface diffusion rate is likely greater than the rate of deposition, leading to the exposure of the most stable {1 1 0) facets as side surfaces, with crystal growth predominantly along the <0 0 2> axis. In support of this hypothesis, a control experiment was performed in which both precursor solutions were fully injected at the first instant of synthesis. As revealed in Figure S3, conventional CsPbBr3 cuboid NCs and a few larger Cs₄PbBr₆ nanocrystals were produced. This result indicates that, under fast reaction conditions, with sufficiently large concentrations of all precursors, the growth at the $\{1\ 1\ 0\}$ and {0 0 2} facets is nearly identical, so that an isometric shape is eventually generated. This interpretation is further supported by the fact that 1-D products were not synthesized in other studies with comparable reaction parameters but with fast precursor injection. 39,44

Yet, adjusting the precursor injection rate is not the sole factor governing the reaction. As discussed in depth in our previous report, it is crucial to manage the interaction between Br and Cs to define reaction outcomes, with much less dependence on the interaction between Br and Pb or between Cs and Pb for the OA-OAm-ODE synthetic system.³³ If any of the precursors are injected individually, one-dimensional CsPbBr3 nanocrystals are not generated. For example, when only Br is slowly introduced to the system, the strong Br-Cs interaction entails that CsBr nanoparticles form first, followed by gradual phase transitions to Cs₄PbBr₆ and eventually to CsPbBr₃ nanocubes.³³ On the contrary, if only the Cs precursor is slowly supplied, two-dimensional CsPbBr3 nanoplatelets result (Figure S4), as has also been demonstrated in other work.³⁹ In this latter case, the local nucleation and atom deposition rates are sufficiently high to result in growth predominantly at both the {0 0 2} and one pair of the {1 1 0} facets.

The growth observed here is fundamentally different from previous reports of anisotropic CsPbBr₃ nanoparticle synthesis, which typically requires special ligands, ^{15,16} preformed nuclei, or undergoes phase transitions. ^{14–16} Moreover, as opposed to semiconductor systems with an isometric crystal symmetry, such as lead chalcogenides, which require oriented attachment or solution-liquid-solid mechanisms for anisotropic growth, 48,49 the production of CsPbBr₃ nanorods in this study appears to depend on the lower symmetry of the crystal lattice. In other words, because the cubic crystal phase of CsPbBr₃ is thermodynamically preferred above 120 °C, ^{19,22} one-dimensional growth is not favored above that reaction temperature. As clearly seen in Figure S5a, samples prepared at 120 °C are a mixture of nanocubes and nanorods having significantly smaller aspect ratios. When the temperature is further raised to 130 and 140 °C (Figure S5b,c), isotropic nanocubes are produced exclusively. This is similar to the morphological transition from platelets to cuboids around 100 °C observed for conventional hot injection syntheses.

Time-Dependent Growth Study. The evolution of nanorods during the course of a 5 min injection was monitored *ex situ*. As shown in Figures 3a, an absorption feature around

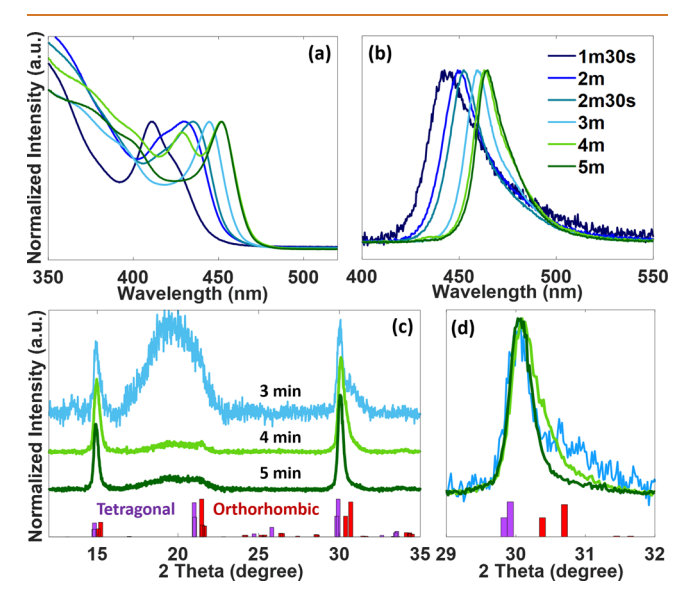


Figure 3. (a) Absorption, (b) PL spectra, and (c and d) XRD patterns of samples collected at different reaction times during a 5 min injection reaction.

410 nm attributed to CsPbBr₃ clusters can be identified at 1 min 30 s.⁵¹ This feature declined at later times, along with the evolution of peaks around 430–435 nm corresponding to nanocrystals with sizes around 2 nm. The absorption peak and absorption edge as well as the PL peak (Figure 3b) red-shifted monotonically as the reaction progressed, indicating growth of the nanocrystals during the time frame of injection. The spectral evolution implies that the growth of nanorods follows a classical mechanism, *i.e.*, generation of clusters that then grow into larger crystals.

The increasing size was confirmed by HRTEM analysis, as depicted in Figure 4 and statistically summarized in Figure 5

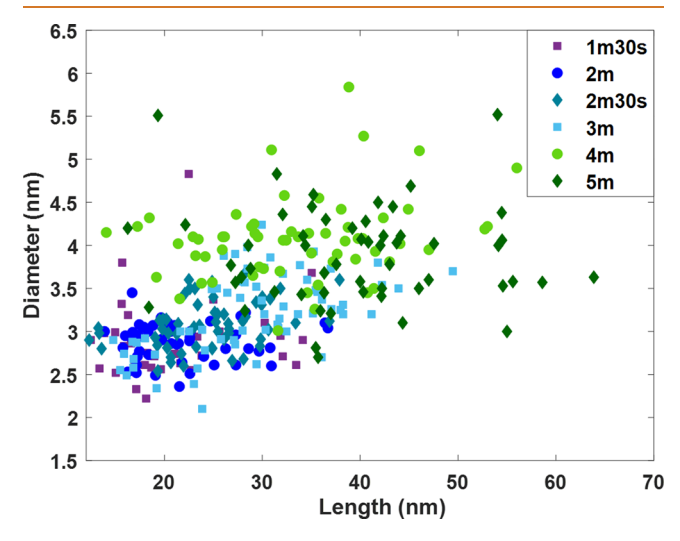


Figure 5. Size statistics of nanorods collected at different reaction times.

Table 1. Average Length and Diameter of Samples Collected at Different Reaction Times^a

sample	length (nm)	diameter (nm)	aspect ratio	fwhm (nm)
1m30s	20.27 ± 6.22	2.91 ± 0.47	6.97	33.94
2m	21.69 ± 5.30	2.88 ± 0.22	7.53	26.97
2m30s	25.22 ± 4.45	3.10 ± 0.29	8.14	23.23
3m	28.96 ± 7.75	3.21 ± 0.46	9.02	21.91
4m	33.54 ± 9.02	4.07 ± 0.48	8.24	22.04
5m	39.32 ± 10.34	3.88 ± 0.57	10.1	21.16

^aThe fwhm is derived from Figure 3b.

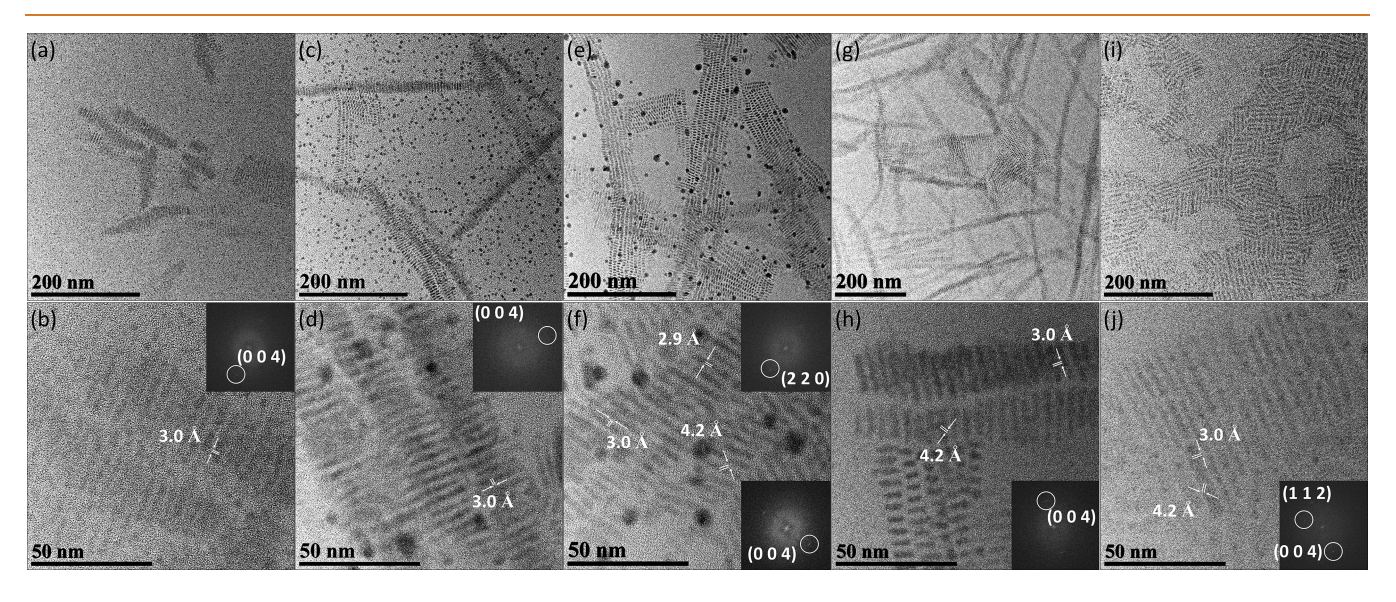


Figure 4. HRTEM images of samples collected at (a and b) 1 min 30 s, (c and d) 2 min, (e and f) 2 min 30 s, (g and h) 3 min, and (i and j) 4 min. Note that the upper panel shows assemblies of the growing nanorods aligned side-by-side. FFTs of individual nanorods are provided in the insets. The 4.2 Å fringes can be assigned to the (1 1 2) plane of tetragonal phase. The samples collected at 1 min 30 s, 2 min, and 2 min 30 s are imaged without purification by centrifugation.

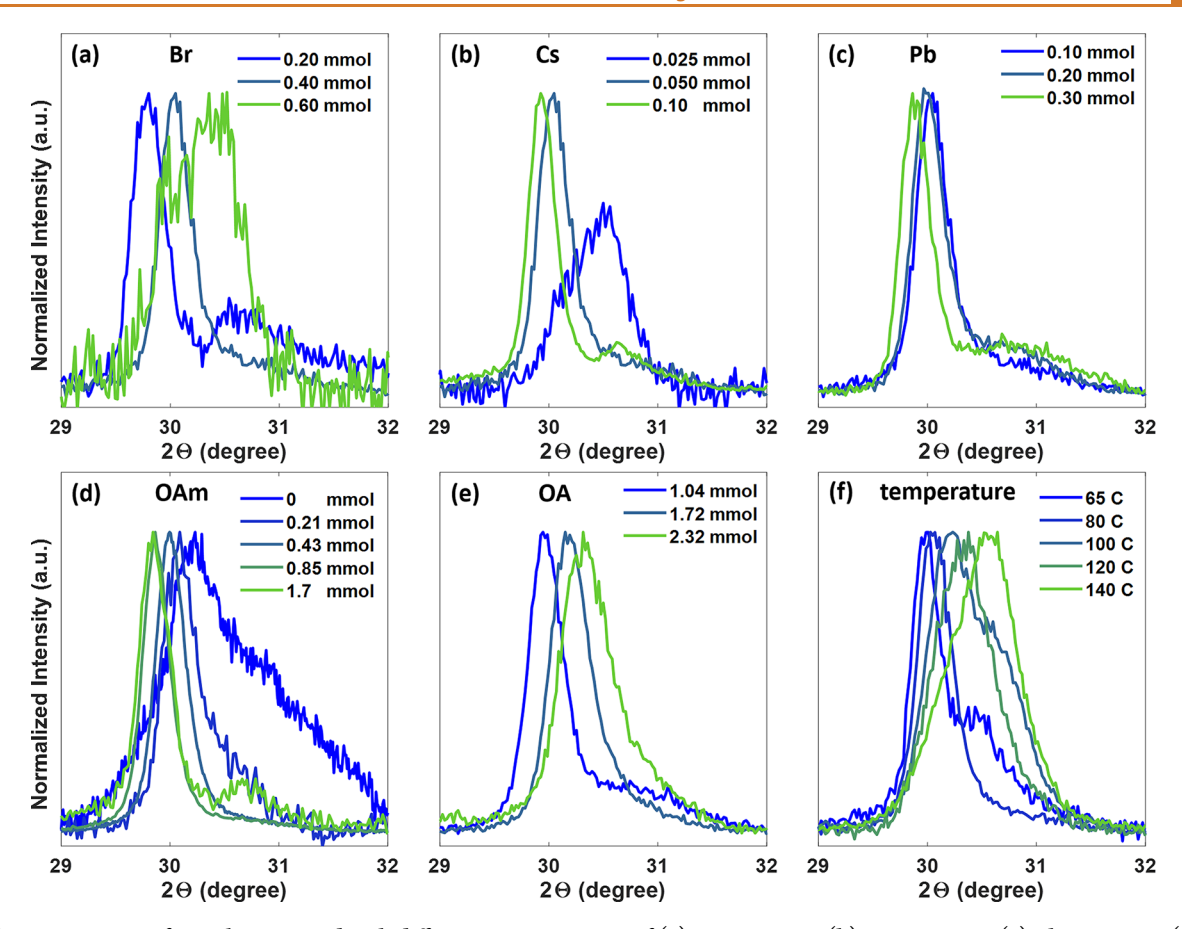


Figure 6. XRD patterns of samples prepared with different concentrations of (a) Br precursor, (b) Cs precursor, (c) Pb precursor, (d) OAm, (e) OA, and (f) at different reaction temperatures. The standard reaction concentrations correspond, respectively, to 0.40, 0.050, 0.10, 0.70, and 2.54 mmol.

and Table 1. Note that, in the HRTEM images, the growing nanorods appear to assemble side-by-side in filament or ribbon-like structures. Samples collected at 1 min 30 s, 2 min, and 2 min 30 s were analyzed as-synthesized, without further purification, due to technical difficulties in isolating early products by centrifugation. The unreacted metal precursors, particularly Pb-oleate, were prone to being reduced by the electron beam forming the dark particles in the images, as also discussed above. For samples collected at 1 min 30 s, the assembled nanorods were already apparent (Figure 4a,b), with diameters focused around 2.9 nm but with a larger distribution in length. At reaction times between 2 and 4 min, multiple assemblies of nanorods with a uniform length were seen (Figure 4c-j). We observed a monotonic elongation from \sim 22 to 33 nm, whereas the average diameter gradually increased from ca. 2.9 to 4.0 nm, leading to an increase in aspect ratio from ca. 7 to 9. No obvious morphological change was noticed after the finish of the injection. These results show a linear relationship between the nanorod size and reaction time such that via a dual slow injection both the size and aspect ratio can be defined. This degree of fine-tuned control over the kinetics of the nanorod growth has not been reported for other synthetic methods that result in one-dimensional CsPbBr₃ nanocrystals.^{8–16} Crucially, this morphological control is obtained in a size regime that promotes quantum confinement (below ~8 nm), which may benefit optical anisotropy and other features of the electronic fine strucure. 52,53

The time evolution was also examined by XRD (Figure 3c,d). Interestingly, the diffraction patterns of samples

collected at 3 min show asymmetric broadening around 15° and 30°. As seen in Figure 3d, the highest intensity peak around 30° and its higher angle shoulder can be assigned to the tetragonal and orthorhombic phases, respectively. The corresponding *d* values were ca. 3.0 and 2.9 Å, which match the values for the lattice spacing measured along the long and short axes during HRTEM analysis (Figure 4 and Figure S6), respectively. As the reaction proceeded to 4 and 5 min, the shoulder gradually disappeared, presenting diffraction patterns close to a pure tetragonal phase. This is consistent with the findings that only lattice spacing around 3.0 Å can be identified along both axes in HRTEM images of the later products. Such lattice expansion during the time evolution and the probable existence of both crystal phases in individual nanocrystals were not commonly observed in other studies. Note that the lattice expansion observed here is opposite to a previous report of size-dependent lattice changes in LHPs, in which the lattice was observed to decrease in size as the NC size increased.⁵⁴ Nonetheless, the XRD analysis suggests that the two phases are compatible, as has been revealed by Whitcher et al.,²⁰ and the phases may readily interconvert during growth. A similar interconvertibility has been reported for the CH₃NH₃PbBr₃ system, with phase transitions from cubic (Pm3m) to tetragonal (I4/mcm) at 236 K and to orthorhombic (Pnma) around 145–149 K. 55,56 This compatibility and interconvertibility can be attributed to the fact that the phases are very similar and are distinguished mostly by the PbBr₃ - sublattice, i.e., the orientation and deformation of [PbBr₆]⁴⁻ octahedra (Figure 2c,d).

Mechanistic Insights into Phase Control. Further experiments with varied concentrations of Br, Cs, Pb, OAm, and OA as well as different reaction temperatures were carried out. A primary finding is that systematic, continuous modification of the crystal lattice between pure tetragonal and pure orthorhombic phases is achieved by modifying reaction parameters (Figure 6 and Figure S7). Further, the one-dimensional nanorod morphology is maintained, independent of the underlying crystal lattice parameters. As displayed in Figure 6a, the major scattering peak monotonically shifts to higher angles with higher Br precursor concentrations, signifying a continuous transformation from the tetragonal to orthorhombic phase. However, opposite trends were observed for Cs and Pb. The peaks shift downward as more metal precursors were supplied (Figure 6b,c). Similar to our previous work,³³ the crystal phase of product appears to be determined by the chemical availability of bromide compared to cesium and lead, where the tetragonal or orthorhombic phases were formed under comparably Br-poor or metal-poor conditions, respectively. In summary, the preference for the crystal phase depends on the magnitude of the following ratio:

$$\frac{[Br]_{eff}}{[Cs]_{eff}[Pb]_{eff}} \tag{1}$$

in which $[Y]_{\rm eff}$ denotes the effective concentration, i.e., the actual number of reactants participating in the chemical reaction.

This inference is further supported by experiments adjusting the ligand concentrations or reaction temperature. It is well-known that additional OAm in the reaction system has a significant influence on Br. By reacting with OA, oleylammonium is produced, further increasing the solubility of bromide in the solution phase: $^{57-59}$

$$R-COOH + R'-NH_2 \leftrightarrow R-COO^- + R'-NH_3^+$$
 (2)

The same effect was noticed in this work. When more OAm was incorporated, the extra oleylammonium stabilized Br in the solution phase and thus decreased its effective concentration for reaction, resulting in the formation of the tetragonal structure (Figure 6d). As for increases in OA concentration, one may anticipate a similar outcome according to Le Chatelier's principle. Nevertheless, we observed an opposite tendency such that the orthorhombic phase became favorable at higher OA concentrations (Figure 6e). This is plausible because additional OA not only shifted the acid-base equilibrium but also raised the solubility of metal ions, particularly the cesium.³⁹ Additionally, OA also likely played a role "activating" the halide. The reaction between OA and oleylammonium halide yields oleylammonium oleate and hydrogen halide, which is an unstable, highly reactive species in the nonpolar solution:

$$R-COOH + R'-NH_3^+X^- \leftrightarrow R-COO^-(NH_3^+)-R' + HX$$
(3)

Apparently, the stabilization of metal ions in the solution phase and the activation of halide were the major outcomes with increased OA. Finally, because of the exothermic acid—base reaction (eq 2), less oleate and oleylammonium, and more OA and OAm are present at higher reaction temperatures. Accordingly, the orthorhombic phase is preferred, as indicated

by the XRD peak shifting to higher angles (Figure 6f) for reactions carried out at a higher temperature.

Overall, when coupling multiple synthetic effects, we notice that the system is more sensitive to the Br/Cs ratio and is less sensitive to the Pb concentration, as also reported in our previous work.³³ With this detailed understanding of the effect of each reaction variable, CsPbBr₃ nanorods with comparable size and shape in nearly pure tetragonal or orthorhombic phases as well as in intermediate lattice configurations were produced by carefully controlling the precursor concentrations (Figures S8 and S9). It is important to emphasize that this synthesis allows for a continuum of lattice parameters in the product nanocrystals, rather than driving the system completely to one phase or the other. That said, some reaction conditions summarized in Figure 6 also appear to promote products with the likely coexistence of both tetragonal and orthorhombic phases. Independent of the diverse crystal lattice geometries, the nanorods exhibited similar overall optical properties, as evaluated by PLQY, fwhm, and by taking the ratio of emission due to suspected localized states versus the emission from free exciton (FE) recombination (Table S1 and Figure S10). This result highlights the consistent, high optical quality of nanorods synthesized via the dual slow injection method, independent of the crystal phase. Further, the continuous lattice modification shows that the two phases are interconvertible, with intermediate configurations that can be isolated.

It is interesting to consider that the conversion between the tetragonal and orthorhombic phases involves two major steps: tilt along the z-coordinate and out-of-phase rotation in the x-y plane of the $[PbBr_6]^{4-}$ octahedron units (Figure 2c,d). The isolation of intermediate phase products indicates that the effective precursor concentrations dictate the lattice geometry, *i.e.*, the degree of octahedra orientation, bond lengths, and bond angles. As mentioned earlier, the rotation and distortion of octahedra units are known to significantly impact the lattice dynamics in LHPs, modifying electronic properties such as the electron—phonon coupling and the exciton binding energy. ^{26,27} Taking advantage of the synthetic control demonstrated here may enable strategies to engineer the charge transport, polaron formation, and related electronic properties that are a consequence of the soft lattice.

Hypothesis for Phase Control. We propose two distinct hypotheses that may explain why the reaction drives the system to the tetragonal or orthorhombic phase: thermodynamic control or kinetic control. Thermodynamic control relates to the dependence of total surface energy on the effective precursor concentrations. As demonstrated computationally, the surface energy of each facet of an orthorhombic CsPbBr₃ crystal changes under Br-rich or Br-poor conditions. 42 In this study, it may be that the {0 0 2} and {1 1 0} facets of an orthorhombic crystal together present lower total surface energy in Br-rich environments, whereas the facets of a tetragonal CsPbBr3 nanocrystal may have a lower surface energy under opposite precursor concentrations. Then, the preference for crystal phase may be a thermodynamic result that minimizes the total surface energy of the crystal, similar to our hypothesis for why the reaction provides a 1-D nanorod morphology.

A kinetic control hypothesis, on the contrary, suggests that the reactivity of monomers determines how the crystal assembles, and this monomer reactivity depends on the coordination strength of the monomer with ligand or solvent

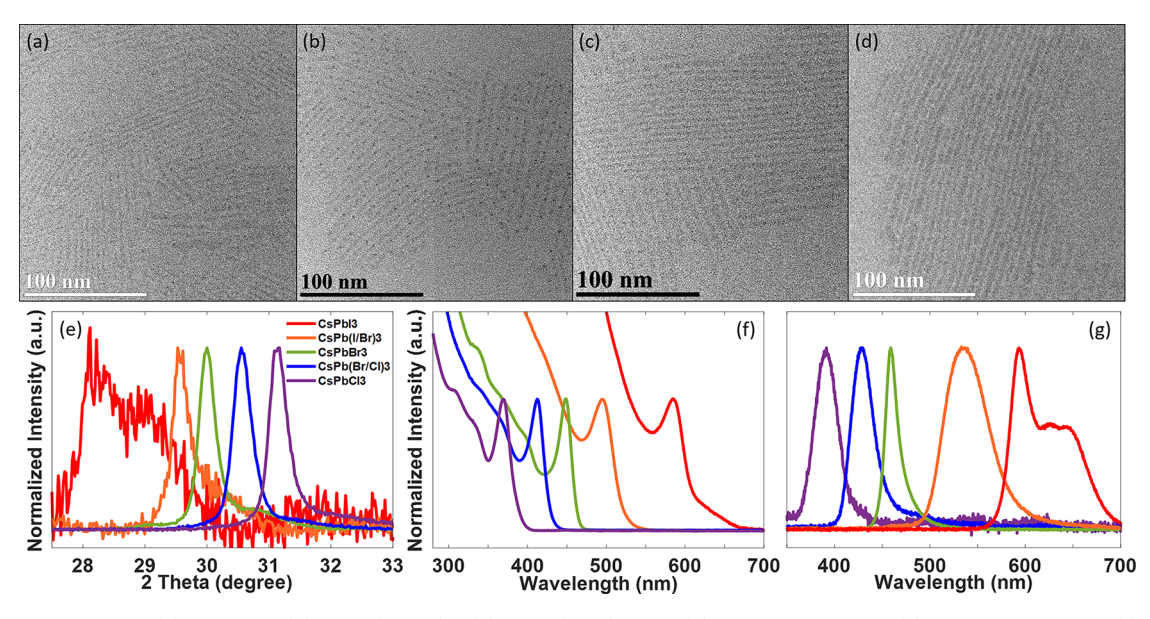


Figure 7. TEM images of (a) CsPbCl₃, (b) CsPb(Br/Cl)₃, (c) CsPb(I/Br)₃, and (d) CsPbI₃ nanorods. (e) XRD patterns and (f) absorption and (g) PL spectra of the corresponding nanorods.

molecules or the local geometry during monomer deposition. For example, Cu₂ZnSnS₄ nanocrystals are produced in the kesterite phase with low reactivity precursors, while a wurtzite phase is promoted using high reactivity precursors.⁶⁰ A similar effect may be expected in this study, as the dependence on effective concentration in eq 1 likely relates to the relative reactivity of the halide or metal monomers. It is well-known that Pb(II) can adopt various coordination numbers, exhibiting different configurations and cluster forms. Specifically, [PbX₆]⁴⁻ octahedra can conjugate with each other through corner-, edge-, and face-sharing, to create 1-D chains, 2-D layers, and 3-D frameworks.⁶¹ In the OA-OAm-ODE system, the formation of two-dimensional olevlammonium bromoplumbate (R'NH₃)₂PbBr₄ has been reported, with higher coordination states $(R'NH_3^+)_n(PbBr_{2+n})^ (n \le 6)$ obtained at higher oleylammonium bromide concentrations. 57,62 Pb(II) can also form Pb-alkylamide species with OAm.⁶³ These species may serve as monomers but with different reactivities and undergoing different reaction mechanisms. Additionally, the chemical environment of metal precursors is dependent on the concentration of ligands. Under high ligand concentrations, metal-ligand pairs surrounded by noncoordinated ligand molecules, namely, reverse micelles, are likely to form.³⁵ Changes in concentrations or temperature can modify the size, density, and even the geometry of reverse micelles, potentially leading to different metal ion reactivities. Overall, the monomer reactivity may be determined by the effective precursor concentrations, kinetically directing the phase of the nanorod crystallization.

To probe our differing hypotheses for the phase selectivity, the thermodynamic stability of nanorods was investigated. At the end of precursor injection, the tetragonal nanorods were aged at the reaction temperature for one additional hour before cleaning. No obvious change was noticed in the nanorod shape (Figure S11a); yet, the main XRD peaks slightly shifted to higher angles after aging (Figure S11c,d). This elucidates that the orthorhombic phase is thermodynamically preferred under the reaction conditions. Moreover, compared to the orthorhombic counterparts, tetragonal CsPbBr₃ nanorods show a poorer stability. As revealed in Figure S12, nanoplatelets were

found in a tetragonal phase sample after two months sitting at room temperature, and the main XRD peaks shifted toward a more orthorhombic character. In comparison, orthorhombic phase samples remained morphologically, structurally, and optically identical after two months (Figure S13). These results strongly suggest that the tetragonal and intermediate phases are metastable, being kinetically trapped and isolated during syntheses. Therefore, it appears that the control over the crystal phase is a consequence of the reaction kinetics, as opposed to thermodynamic driving forces and that precursor reactivity is likely responsible for modifying the PbBr₃⁻ sublattice geometry. In contrast, the growth direction of the crystal lattice and the resulting 1-D shape appear to be determined thermodynamically, as discussed above. Thus, it seems that overall nanocrystal growth is dictated by kinetic or thermodynamic mechanisms at different growth scales.

Extension to Other Halide Systems. Finally, we show that the synthetic strategy behaves similarly when the oleylammonium halide precursor is a chloride or iodide. As displayed in Figure 7a-e, CsPbX₃ nanorods with various halide compositions were successfully prepared when the molar ratio of the respective halides was included in the precursor injection step. In particular, the chloride and mixed halide samples share the same optical features as the CsPbBr₃ nanorods: a sharp absorption edge, strong excitonic absorption peak, and asymmetric PL emission (Figure 7f,g). The XRD patterns of the chloride and iodide nanorods (Figure S14), surprisingly again, exhibit crystal structures that cannot be assigned to any of the commonly observed cubic, orthorhombic, or P4mm tetragonal phases. Additionally, the crystal phase of the CsPbCl₃ nanorods is continuously tuned between the orthorhombic phase and the unknown phase via modification of the reaction parameters, and the phase preference follows the same rule that was established in the bromide system (eq 1). Considering this, we suspect that the unknown crystal structures identified for the CsPbCl3 and CsPbI₃ nanorods are analogous to the tetragonal CsPbBr₃ nanorods with I4/mcm symmetry. Accordingly, XRD diffractograms for CsPbCl₃ and CsPbI₃ with I4/mcm structures have been simulated (Figure S14a and Table S2), and the patterns

match well with the experimental scattering patterns. In further support of our interpretation, the lattice parameters of mixed halide nanorods correspond as expected for the predicted stoichiometry on the basis of the molar ratio of halides in the injection step (Figure S15 and Table S3). Thus, the dual slow injection method provides 1-D growth and crystal phase tunability as well as excellent control over the halide composition for the entire CsPbX₃ system.

CONCLUSION

In conclusion, we have reported a synthetic strategy based on the simultaneous, slow injection of separate Cs and halide precursors. The synthesis can be used to tailor the shape, size, and crystal phase of CsPbX₃ perovskite nanocrystals across a size regime that provides quantum confinement, and the method is generally applicable for pure and mixed halide compositions based on Cl, Br, or I. A one-dimensional nanorod morphology is produced when the synthesis is performed at decreased temperature because of the thermodynamic preference of the system for a lower symmetry crystal structure. Further, the crystal phase is continuously tunable between an orthorhombic or tetragonal (I4/mcm) structure, with the ability to control the overall nanorod morphology and aspect ratio independently of the underlying lattice structure. The preference for lattice structure is determined kinetically by the effective concentrations of the three precursor species. Under comparably halide-poor and metal-rich conditions, the tetragonal phase is preferred, whereas the orthorhombic phase is preferred under opposite conditions. This slow injection strategy offers excellent synthetic control compared with other reports for the preparation of CsPbX₃ perovskite nanocrystals with anisotropic morphologies, and the key innovation of our strategy, i.e., an effective method to significantly slow the kinetics of the growing crystal, may be extended to achieve more sophisticated chemical and structural designs in the materials system.

METHODS

Materials. Cs₂CO₃ (99.9%), PbO (99%), oleic acid (OA, 90%), oleylamine (OAm, 70%), 1-octadecene (ODE, 90%), toluene (99.8%), and hexane (95%) were received from Sigma-Aldrich. Hydrobromic acid (HBr, 48%) was purchased from VWR Chemicals BDH. Hydrochloric acid (HCl, 36.5–38%) was purchased from Macron Fine Chemicals. Hydriodic acid (HI, 55–58%) was purchased from Thermo Scientific. OA and OAm were dried with molecular sieves under an Ar environment before use. Other chemicals were used as received.

Preparation of Cesium Oleate (Cs-OA) Stock Solution. Cs_2CO_3 (0.2 g) was reacted with 0.6 mL of OA in 10 mL of ODE at 120 $^{\circ}C$ under a vacuum for 1 h. Once the chemical was dissolved, an additional 1.6 mL of OA was added under an Ar atmosphere, and the solution was allowed to cool down to room temperature and transferred to an Ar-filled vial for storage.

Preparation of Lead Oleate (Pb-OA) Stock Solution. PbO (0.185~g) was loaded into a 25 mL flask along with 4.3 mL of ODE and 0.64 mL of OA, and the mixture was dried at 125 $^{\circ}$ C under a vacuum for 1.5 h until the chemical was fully solubilized.

Preparation of Oleylammonium Halide (OAm-X). Ten milliliters of undried OAm was added in 30 mL of acetonitrile under vigorous stirring in an Ar-filled, covered beaker. A specific amount of HX (3.5 mL for HCl; 4 mL for HBr; 5 mL for HI) was then injected drop by drop into the solution, which was cooled in a water bath. The solution was stirred for an additional hour (overnight for HI) with Ar purging. The precipitate was then purified with

diethyl ether and hexane several times, dried under a vacuum at 60 $^{\circ}\text{C}$ overnight, and stored in a glovebox for future use.

Synthesis of CsPbBr₃ via Slow Injection of Precursors. In a typical slow injection synthesis, 5 mL of ODE was loaded into a round bottom flask and dried under a vacuum at 120 °C. It was allowed to cool down to 80 °C, and 0.3 mL of Pb-OA stock solution was injected. To prepare the Cs feedstock, 0.3 mL of Cs-OA stock solution was mixed with 0.55 mL of OA, 0.25 mL of OAm, and 0.27 mL of ODE. Separately, 0.085 g of OAm-Br was mixed with 0.65 mL of toluene and 0.45 mL of ODE. The two feedstock solutions were individually injected into the flask, at a rate of 10.8 mL/h or slower with an amount of 0.9 mL each. The sample was purified by centrifugation at 8000 rcf for 15 min. The supernatant was discarded, and the precipitate was redispersed in hexane and centrifuged at 3000 rcf for another 10 min. The final supernatant was collected for future ranalysis. For the time-dependent studies, samples were prepared by quenching the reaction at different time intervals in separate reaction batches.

Characterization. XRD data was measured on a BRUKER D8-Focus Bragg—Brentano X-ray powder diffractometer equipped with a Cu K α radiation source. Absorption and PL spectra were collected on an Ocean Optics Flame-S-UV—vis spectrometer with an Ocean Optics DH-200-Bal deuterium lamp light source. HRTEM images were taken on a FEI Tecnai G2 F20 ST FE-TEM operated at 200 kV equipped with a Gatan CCD camera. PLE measurements were performed on a home-built L-format optical setup equipped with a broadband supercontinuum laser light source (Fianium Limited SC4 \times 0) as depicted in Scheme S1. The excitation beam was attenuated using a variable neutral density filter (Thorlabs NDC-25C-2) prior to exciting the sample. The PL emission from the sample was collected perpendicular to the excitation beam using an optical fiber attached to the cuvette holder and resolved with an Ocean Optics Flame-S-UV—vis spectrometer.

XRD Diffractogram Simulation. The powder XRD patterns of CsPbCl₃ and CsPbI₃ with I4/mcm symmetry were calculated using the software package VESTA. The lattice parameters were estimated on the basis of the ratios of lattice constants of the corresponding cubic $(Pm\bar{3}m)$ phases.

ASSOCIATED CONTENT

Supporting Information

The Supporting Information is available free of charge at https://pubs.acs.org/doi/10.1021/acsnano.2c02474.

Figures of HRTEM images, 2D PLE contour map, absorbance and PL emission spectra, UV—vis spectra, XRD patterns, LSE/FE ratio as a function of XRD peak position, XRD card files, scheme of experimental setup for PLE measurement, tables of PLQY and FWHM of tetragonal and orthorhombic nanorods, lattice constants, and XRD peak positions of CsPbX₃ nanorods with varied Br/Cl compositions (PDF)

AUTHOR INFORMATION

Corresponding Author

Matthew T. Sheldon — Department of Chemistry, Texas A&M University, College Station, Texas 77843-3255, United States; Department of Materials Science & Engineering, Texas A&M University, College Station, Texas 77843-3255, United States; orcid.org/0000-0002-4940-7966; Email: sheldonm@tamu.edu

Authors

Je-Ruei Wen — Department of Chemistry, Texas A&M University, College Station, Texas 77843-3255, United States; Occid.org/0000-0002-1602-5021 Freddy Alberto Rodríguez Ortiz — Department of Chemistry, Texas A&M University, College Station, Texas 77843-3255, United States; orcid.org/0000-0001-8289-2281

Anna Champ — Department of Chemistry, Texas A&M University, College Station, Texas 77843-3255, United States

Complete contact information is available at: https://pubs.acs.org/10.1021/acsnano.2c02474

Author Contributions

J.-R.W. designed and conducted the experiments with some help from A.C. F.A.R.O. performed the PLE characterization. J.-R.W., F.A.R.O., and M.T.S. wrote the manuscript. All authors reviewed the manuscript.

Notes

The authors declare no competing financial interest.

ACKNOWLEDGMENTS

This work was funded in part by the National Science Foundation (Grant DMR-2131408). M.T.S. also acknowledges support from the Welch Foundation (A-1886). The authors also acknowledge technical support for HRTEM imaging from Texas A&M University Microscopy and Imaging Center Core Facility (RRID:SCR_022128).

REFERENCES

- (1) Dey, A.; Ye, J.; De, A.; Debroye, E.; Ha, S. K.; Bladt, E.; Kshirsagar, A. S.; Wang, Z.; Yin, J.; Wang, Y.; Quan, L. N.; Yan, F.; Gao, M.; Li, X.; Shamsi, J.; Debnath, T.; Cao, M.; Scheel, M. A.; Kumar, S.; Steele, J. A.; Gerhard, M.; Chouhan, L.; Xu, K.; Wu, X.-g.; Li, Y.; Zhang, Y.; Dutta, A.; Han, C.; Vincon, I.; Rogach, A. L.; Nag, A.; Samanta, A.; Korgel, B. A.; Shih, C.-J.; Gamelin, D. R.; Son, D. H.; Zeng, H.; Zhong, H.; Sun, H.; Demir, H. V.; Scheblykin, I. G.; Mora-Seró, I.; Stolarczyk, J. K.; Zhang, J. Z.; Feldmann, J.; Hofkens, J.; Luther, J. M.; Pérez-Prieto, J.; Li, L.; Manna, L.; Bodnarchuk, M. I.; Kovalenko, M. V.; Roeffaers, M. B. J.; Pradhan, N.; Mohammed, O. F.; Bakr, O. M.; Yang, P.; Müller-Buschbaum, P.; Kamat, P. V.; Bao, Q.; Zhang, Q.; Krahne, R.; Galian, R. E.; Stranks, S. D.; Bals, S.; Biju, V.; Tisdale, W. A.; Yan, Y.; Hoye, R. L. Z.; Polavarapu, L. State of the Art and Prospects for Halide Perovskite Nanocrystals. ACS Nano 2021, 15 (7), 10775–10981.
- (2) Hu, J.; Li, L.-s.; Yang, W.; Manna, L.; Wang, L.-w.; Alivisatos, A. P. Linearly Polarized Emission from Colloidal Semiconductor Quantum Rods. *Science* **2001**, 292 (5524), 2060–2063.
- (3) Cunningham, P. D.; Souza, J. B.; Fedin, I.; She, C.; Lee, B.; Talapin, D. V. Assessment of Anisotropic Semiconductor Nanorod and Nanoplatelet Heterostructures with Polarized Emission for Liquid Crystal Display Technology. ACS Nano 2016, 10 (6), 5769–5781.
- (4) Wu, K.; Zhu, H.; Liu, Z.; Rodríguez-Córdoba, W.; Lian, T. Ultrafast Charge Separation and Long-Lived Charge Separated State in Photocatalytic CdS-Pt Nanorod Heterostructures. *J. Am. Chem. Soc.* **2012**, *134* (25), 10337–10340.
- (5) Martin, J.; Ratnaweera, R.; Kumar, S.; Wen, J.-R.; Kutayiah, A. R.; Sheldon, M. Detailed balance efficiencies for luminescent solar concentrators with aligned semiconductor nanorods: the benefits of anisotropic emission. *J. Photonics Energy* **2020**, *10* (2), 025501.
- (6) Kutayiah, A. R.; Kumar, S.; Ratnaweera, R.; Easwaran, K.; Sheldon, M. Markov chains for modeling complex luminescence, absorption, and scattering in nanophotonic systems. *Opt. Express* **2021**, 29 (3), 4249–4269.
- (7) Ratnaweera, R. J.; Rodríguez Ortiz, F. A.; Gripp, N. J.; Sheldon, M. T. Quantifying Order during Field-Driven Alignment of Colloidal Semiconductor Nanorods. *ACS Nano* **2022**, *16* (3), 3834–3842.
- (8) Li, Y.; Huang, H.; Xiong, Y.; Richter, A. F.; Kershaw, S. V.; Feldmann, J.; Rogach, A. L. Using Polar Alcohols for the Direct Synthesis of Cesium Lead Halide Perovskite Nanorods with Anisotropic Emission. *ACS Nano* **2019**, *13* (7), 8237–8245.

- (9) Leng, J.; Wang, T.; Zhao, X.; Ong, E. W. Y.; Zhu, B.; Ng, J. D. A.; Wong, Y.-C.; Khoo, K. H.; Tamada, K.; Tan, Z.-K. Thermodynamic Control in the Synthesis of Quantum-Confined Blue-Emitting CsPbBr3 Perovskite Nanostrips. *J. Phys. Chem. Lett.* **2020**, *11* (6), 2036–2043.
- (10) Tong, Y.; Fu, M.; Bladt, E.; Huang, H.; Richter, A. F.; Wang, K.; Müller-Buschbaum, P.; Bals, S.; Tamarat, P.; Lounis, B.; Feldmann, J.; Polavarapu, L. Chemical Cutting of Perovskite Nanowires into Single-Photon Emissive Low-Aspect-Ratio CsPbX₃ (X = Cl, Br, I) Nanorods. *Angew. Chem., Int. Ed.* **2018**, *57* (49), 16094–16098.
- (11) Mehetor, S. K.; Ghosh, H.; Pradhan, N. Blue-Emitting CsPbBr₃ Perovskite Quantum Rods and Their Wide-Area 2D Self-Assembly. *ACS Energy Lett.* **2019**, *4* (6), 1437–1442.
- (12) Bera, S.; Shyamal, S.; Pradhan, N. Chemically Spiraling CsPbBr₃ Perovskite Nanorods. *J. Am. Chem. Soc.* **2021**, 143 (36), 14895–14906.
- (13) Hudait, B.; Dutta, S. K.; Bera, S.; Pradhan, N. Introducing B-Site Cations by Ion Exchange and Shape Anisotropy in CsPbBr₃ Perovskite Nanostructures. *Nano Lett.* **2021**, 21 (12), 5277–5284.
- (14) Yang, D.; Li, P.; Zou, Y.; Cao, M.; Hu, H.; Zhong, Q.; Hu, J.; Sun, B.; Duhm, S.; Xu, Y.; Zhang, Q. Interfacial Synthesis of Monodisperse CsPbBr₃ Nanorods with Tunable Aspect Ratio and Clean Surface for Efficient Light-Emitting Diode Applications. *Chem. Mater.* **2019**, *31* (5), 1575–1583.
- (15) Jing, Q.; Su, Y.; Xing, X.; Lu, Z. Highly luminescent CsPbBr₃ nanorods synthesized by a ligand-regulated reaction at the water-oil interface. *J. Mater. Chem. C* **2019**, 7 (7), 1854–1858.
- (16) Wang, S.; Yu, J.; Zhang, M.; Chen, D.; Li, C.; Chen, R.; Jia, G.; Rogach, A. L.; Yang, X. Stable, Strongly Emitting Cesium Lead Bromide Perovskite Nanorods with High Optical Gain Enabled by an Intermediate Monomer Reservoir Synthetic Strategy. *Nano Lett.* **2019**, *19* (9), 6315–6322.
- (17) Pradhan, N. Do Halide Perovskites Prefer a Specific Direction for Forming One-Dimensional Nanostructures? *ACS Energy Lett.* **2022**, *7* (1), 150–153.
- (18) Steele, J. A.; Lai, M.; Zhang, Y.; Lin, Z.; Hofkens, J.; Roeffaers, M. B. J.; Yang, P. Phase Transitions and Anion Exchange in All-Inorganic Halide Perovskites. *Acc. Mater. Res.* **2020**, *1* (1), 3–15.
- (19) dos Reis, R.; Yang, H.; Ophus, C.; Ercius, P.; Bizarri, G.; Perrodin, D.; Shalapska, T.; Bourret, E.; Ciston, J.; Dahmen, U. Determination of the structural phase and octahedral rotation angle in halide perovskites. *Appl. Phys. Lett.* **2018**, *112* (7), 071901.
- (20) Whitcher, T. J.; Gomes, L. C.; Zhao, D.; Bosman, M.; Chi, X.; Wang, Y.; Carvalho, A.; Hui, H. K.; Chang, Q.; Breese, M. B. H.; Castro Neto, A. H.; Wee, A. T. S.; Sun, H. D.; Chia, E. E. M.; Rusydi, A. Dual phases of crystalline and electronic structures in the nanocrystalline perovskite CsPbBr₃. NPG Asia Mater. **2019**, 11 (1), 70.
- (21) Stoumpos, C. C.; Malliakas, C. D.; Peters, J. A.; Liu, Z.; Sebastian, M.; Im, J.; Chasapis, T. C.; Wibowo, A. C.; Chung, D. Y.; Freeman, A. J.; Wessels, B. W.; Kanatzidis, M. G. Crystal Growth of the Perovskite Semiconductor CsPbBr₃: A New Material for High-Energy Radiation Detection. *Cryst. Growth Des.* **2013**, *13* (7), 2722–2727.
- (22) Cottingham, P.; Brutchey, R. L. Depressed Phase Transitions and Thermally Persistent Local Distortions in CsPbBr₃ Quantum Dots. *Chem. Mater.* **2018**, *30* (19), *6711–6716*.
- (23) Xue, J.; Yang, D.; Cai, B.; Xu, X.; Wang, J.; Ma, H.; Yu, X.; Yuan, G.; Zou, Y.; Song, J.; Zeng, H. Photon-Induced Reversible Phase Transition in CsPbBr₃ Perovskite. *Adv. Funct. Mater.* **2019**, 29 (13), 1807922.
- (24) Yu, Y.; Zhang, D.; Kisielowski, C.; Dou, L.; Kornienko, N.; Bekenstein, Y.; Wong, A. B.; Alivisatos, A. P.; Yang, P. Atomic Resolution Imaging of Halide Perovskites. *Nano Lett.* **2016**, *16* (12), 7530–7535.
- (25) Hussain, M.; Rashid, M.; Saeed, F.; Bhatti, A. S. Spin-orbit coupling effect on energy level splitting and band structure inversion in CsPbBr₃. *J. Mater. Sci.* **2021**, *56* (1), 528–542.

- (26) Herz, L. M. How Lattice Dynamics Moderate the Electronic Properties of Metal-Halide Perovskites. *J. Phys. Chem. Lett.* **2018**, 9 (23), 6853–6863.
- (27) Miyata, K.; Meggiolaro, D.; Trinh, M. T.; Joshi, P. P.; Mosconi, E.; Jones, S. C.; De Angelis, F.; Zhu, X.-Y. Large polarons in lead halide perovskites. *Sci. Adv.* **2017**, 3 (8), No. e1701217.
- (28) Lignos, I.; Stavrakis, S.; Nedelcu, G.; Protesescu, L.; deMello, A. J.; Kovalenko, M. V. Synthesis of Cesium Lead Halide Perovskite Nanocrystals in a Droplet-Based Microfluidic Platform: Fast Parametric Space Mapping. *Nano Lett.* **2016**, *16* (3), 1869–1877.
- (29) Protesescu, L.; Yakunin, S.; Bodnarchuk, M. I.; Krieg, F.; Caputo, R.; Hendon, C. H.; Yang, R. X.; Walsh, A.; Kovalenko, M. V. Nanocrystals of Cesium Lead Halide Perovskites (CsPbX₃, X = Cl, Br, and I): Novel Optoelectronic Materials Showing Bright Emission with Wide Color Gamut. *Nano Lett.* **2015**, *15* (6), 3692–3696.
- (30) Krieg, F.; Sercel, P. C.; Burian, M.; Andrusiv, H.; Bodnarchuk, M. I.; Stöferle, T.; Mahrt, R. F.; Naumenko, D.; Amenitsch, H.; Rainò, G.; Kovalenko, M. V. Monodisperse Long-Chain Sulfobetaine-Capped CsPbBr₃ Nanocrystals and Their Superfluorescent Assemblies. ACS Cent. Sci. 2021, 7 (1), 135–144.
- (31) Xia, Y.; Xia, X.; Peng, H.-C. Shape-Controlled Synthesis of Colloidal Metal Nanocrystals: Thermodynamic versus Kinetic Products. J. Am. Chem. Soc. 2015, 137 (25), 7947–7966.
- (32) Chang, J.; Waclawik, E. R. Colloidal semiconductor nanocrystals: controlled synthesis and surface chemistry in organic media. *RSC Adv.* **2014**, *4* (45), 23505–23527.
- (33) Wen, J.-R.; Roman, B. J.; Rodriguez Ortiz, F. A.; Mireles Villegas, N.; Porcellino, N.; Sheldon, M. Chemical Availability of Bromide Dictates CsPbBr₃ Nanocrystal Growth. *Chem. Mater.* **2019**, 31 (20), 8551–8557.
- (34) Dang, Z.; Shamsi, J.; Palazon, F.; Imran, M.; Akkerman, Q. A.; Park, S.; Bertoni, G.; Prato, M.; Brescia, R.; Manna, L. In Situ Transmission Electron Microscopy Study of Electron Beam-Induced Transformations in Colloidal Cesium Lead Halide Perovskite Nanocrystals. ACS Nano 2017, 11 (2), 2124–2132.
- (35) Ferreira, D. L.; Sousa, J. C. L.; Maronesi, R. N.; Bettini, J.; Schiavon, M. A.; Teixeira, A. V. N. C.; Silva, A. G. Size-dependent bandgap and particle size distribution of colloidal semiconductor nanocrystals. *J. Chem. Phys.* **2017**, *147* (15), 154102.
- (36) Yu, W. W.; Qu, L.; Guo, W.; Peng, X. Experimental Determination of the Extinction Coefficient of CdTe, CdSe, and CdS Nanocrystals. *Chem. Mater.* **2003**, *15* (14), 2854–2860.
- (37) Akkerman, Q. A.; Motti, S. G.; Srimath Kandada, A. R.; Mosconi, E.; D'Innocenzo, V.; Bertoni, G.; Marras, S.; Kamino, B. A.; Miranda, L.; De Angelis, F.; Petrozza, A.; Prato, M.; Manna, L. Solution Synthesis Approach to Colloidal Cesium Lead Halide Perovskite Nanoplatelets with Monolayer-Level Thickness Control. J. Am. Chem. Soc. 2016, 138 (3), 1010–1016.
- (38) Zhang, D. D.; Yu, Y.; Bekenstein, Y.; Wong, A. B.; Alivisatos, A. P.; Yang, P. D. Ultrathin Colloidal Cesium Lead Halide Perovskite Nanowires. *J. Am. Chem. Soc.* **2016**, *138* (40), 13155–13158.
- (39) Lu, C.; Wright, M. W.; Ma, X.; Li, H.; Itanze, D. S.; Carter, J. A.; Hewitt, C. A.; Donati, G. L.; Carroll, D. L.; Lundin, P. M.; Geyer, S. M. Cesium Oleate Precursor Preparation for Lead Halide Perovskite Nanocrystal Synthesis: The Influence of Excess Oleic Acid on Achieving Solubility, Conversion, and Reproducibility. *Chem. Mater.* **2019**, *31* (1), 62–67.
- (40) Wu, X.; Trinh, M. T.; Niesner, D.; Zhu, H.; Norman, Z.; Owen, J. S.; Yaffe, O.; Kudisch, B. J.; Zhu, X. Y. Trap States in Lead Iodide Perovskites. *J. Am. Chem. Soc.* **2015**, *137* (5), 2089–2096.
- (41) Ma, X.; Shen, P.; Wang, Y.-N.; Pan, F.; Chen, G.; Xu, S.; Ye, H. Local Phonon Modes Concerned with the Self-Trapped Exciton State in CsPbBr₃ Nanocrystals. *J. Phys. Chem. C* **2020**, *124* (49), 27130–27135
- (42) Peng, L.; Dutta, S. K.; Mondal, D.; Hudait, B.; Shyamal, S.; Xie, R.; Mahadevan, P.; Pradhan, N. Arm Growth and Facet Modulation in Perovskite Nanocrystals. *J. Am. Chem. Soc.* **2019**, *141* (40), 16160–16168.

- (43) Bertolotti, F.; Nedelcu, G.; Vivani, A.; Cervellino, A.; Masciocchi, N.; Guagliardi, A.; Kovalenko, M. V. Crystal Structure, Morphology, and Surface Termination of Cyan-Emissive, Six-Monolayers-Thick CsPbBr₃ Nanoplatelets from X-ray Total Scattering. ACS Nano 2019, 13 (12), 14294–14307.
- (44) Bekenstein, Y.; Koscher, B. A.; Eaton, S. W.; Yang, P.; Alivisatos, A. P. Highly Luminescent Colloidal Nanoplates of Perovskite Cesium Lead Halide and Their Oriented Assemblies. *J. Am. Chem. Soc.* **2015**, *137* (51), 16008–16011.
- (45) Shamsi, J.; Dang, Z.; Bianchini, P.; Canale, C.; Di Stasio, F.; Brescia, R.; Prato, M.; Manna, L. Colloidal Synthesis of Quantum Confined Single Crystal CsPbBr3 Nanosheets with Lateral Size Control up to the Micrometer Range. *J. Am. Chem. Soc.* **2016**, *138* (23), 7240–7243.
- (46) Dong, Y.; Qiao, T.; Kim, D.; Parobek, D.; Rossi, D.; Son, D. H. Precise Control of Quantum Confinement in Cesium Lead Halide Perovskite Quantum Dots via Thermodynamic Equilibrium. *Nano Lett.* **2018**, *18* (6), 3716–3722.
- (47) Imran, M.; Ijaz, P.; Baranov, D.; Goldoni, L.; Petralanda, U.; Akkerman, Q.; Abdelhady, A. L.; Prato, M.; Bianchini, P.; Infante, I.; Manna, L. Shape-Pure, Nearly Monodispersed CsPbBr₃ Nanocubes Prepared Using Secondary Aliphatic Amines. *Nano Lett.* **2018**, *18* (12), 7822–7831.
- (48) Kershaw, S. V.; Susha, A. S.; Rogach, A. L. Narrow bandgap colloidal metal chalcogenide quantum dots: synthetic methods, heterostructures, assemblies, electronic and infrared optical properties. *Chem. Soc. Rev.* **2013**, *42* (7), 3033–3087.
- (49) Wang, F.; Dong, A.; Buhro, W. E. Solution-Liquid-Solid Synthesis, Properties, and Applications of One-Dimensional Colloidal Semiconductor Nanorods and Nanowires. *Chem. Rev.* **2016**, *116* (18), 10888–10933.
- (50) Otero-Martínez, C.; García-Lojo, D.; Pastoriza-Santos, I.; Pérez-Juste, J.; Polavarapu, L. Dimensionality Control of Inorganic and Hybrid Perovskite Nanocrystals by Reaction Temperature: From No-Confinement to 3D and 1D Quantum Confinement. *Angew. Chem., Int. Ed.* **2021**, *60* (51), 26677–26684.
- (51) Peng, L.; Dutta, A.; Xie, R.; Yang, W.; Pradhan, N. Dot-Wire-Platelet-Cube: Step Growth and Structural Transformations in CsPbBr₃ Perovskite Nanocrystals. *ACS Energy Lett.* **2018**, 3 (8), 2014–2020.
- (52) Zhao, X.; Wei, C. M.; Yang, L.; Chou, M. Y. Quantum Confinement and Electronic Properties of Silicon Nanowires. *Phys. Rev. Lett.* **2004**, 92 (23), 236805.
- (53) Matsui, H.; Tabata, H. The contribution of quantum confinement to optical anisotropy of a-plane Cd_{0.06}Zn_{0.94}O/ZnO quantum wells. *Appl. Phys. Lett.* **2012**, *100* (17), 171910.
- (54) Zhao, Q.; Hazarika, A.; Schelhas, L. T.; Liu, J.; Gaulding, E. A.; Li, G.; Zhang, M.; Toney, M. F.; Sercel, P. C.; Luther, J. M. Size-Dependent Lattice Structure and Confinement Properties in CsPbI₃ Perovskite Nanocrystals: Negative Surface Energy for Stabilization. *ACS Energy Lett.* **2020**, *5* (1), 238–247.
- (55) Anusca, I.; Balčiũnas, S.; Gemeiner, P.; Svirskas, Š.; Sanlialp, M.; Lackner, G.; Fettkenhauer, C.; Belovickis, J.; Samulionis, V.; Ivanov, M.; Dkhil, B.; Banys, J.; Shvartsman, V. V.; Lupascu, D. C. Dielectric Response: Answer to Many Questions in the Methylammonium Lead Halide Solar Cell Absorbers. *Adv. Energy Mater.* 2017, 7 (19), 1700600.
- (56) Poglitsch, A.; Weber, D. Dynamic disorder in methylammoniumtrihalogenoplumbates (II) observed by millimeter-wave spectroscopy. *J. Chem. Phys.* **1987**, *87* (11), 6373–6378.
- (57) Almeida, G.; Goldoni, L.; Akkerman, Q.; Dang, Z.; Khan, A. H.; Marras, S.; Moreels, I.; Manna, L. Role of Acid-Base Equilibria in the Size, Shape, and Phase Control of Cesium Lead Bromide Nanocrystals. *ACS Nano* **2018**, *12* (2), 1704–1711.
- (58) Liu, Z. K.; Bekenstein, Y.; Ye, X. C.; Nguyen, S. C.; Swabeck, J.; Zhang, D. D.; Lee, S. T.; Yang, P. D.; Ma, W. L.; Alivisatos, A. P. Ligand Mediated Transformation of Cesium Lead Bromide Perovskite Nanocrystals to Lead Depleted Cs₄PbBr₆ Nanocrystals. *J. Am. Chem. Soc.* **2017**, *139* (15), 5309–5312.

- (59) Udayabhaskararao, T.; Houben, L.; Cohen, H.; Menahem, M.; Pinkas, I.; Avram, L.; Wolf, T.; Teitelboim, A.; Leskes, M.; Yaffe, O.; Oron, D.; Kazes, M. A Mechanistic Study of Phase Transformation in Perovskite Nanocrystals Driven by Ligand Passivation. *Chem. Mater.* **2018**, *30* (1), 84–93.
- (60) Zou, Y.; Su, X.; Jiang, J. Phase-Controlled Synthesis of Cu₂ZnSnS₄ Nanocrystals: The Role of Reactivity between Zn and S. J. Am. Chem. Soc. **2013**, 135 (49), 18377–18384.
- (61) Lei, X.-W.; Yue, C.-Y.; Wei, J.-C.; Li, R.-Q.; Li, Y.; Mi, F.-Q. Transition metal complex directed lead bromides with tunable structures and visible light driven photocatalytic properties. *Dalton Trans.* **2016**, *45* (48), 19389–19398.
- (62) Grisorio, R.; Fanizza, E.; Allegretta, I.; Altamura, D.; Striccoli, M.; Terzano, R.; Giannini, C.; Vergaro, V.; Ciccarella, G.; Margiotta, N.; Suranna, G. P. Insights into the role of the lead/surfactant ratio in the formation and passivation of cesium lead bromide perovskite nanocrystals. *Nanoscale* **2020**, *12* (2), 623–637.
- (63) Kerner, R. A.; Schloemer, T. H.; Schulz, P.; Berry, J. J.; Schwartz, J.; Sellinger, A.; Rand, B. P. Amine additive reactions induced by the soft Lewis acidity of Pb²⁺ in halide perovskites. Part I: evidence for Pb-alkylamide formation. *J. Mater. Chem. C* **2019**, 7 (18), 5251–5259.

☐ Recommended by ACS

Stable CsPbBr₃ Nanoclusters Feature a Disk-like Shape and a Distorted Orthorhombic Structure

Baowei Zhang, Liberato Manna, et al.

MARCH 08, 2022

JOURNAL OF THE AMERICAN CHEMICAL SOCIETY

READ 🗹

Tailoring CsPbBr₃ Growth via Non-Polar Solvent Choice and Heating Methods

Hediyeh Zamani, Mathew M. Maye, et al.

JULY 21, 2022

LANGMUIR

READ 🗹

Cs-Lattice Extension and Expansion for Inducing Secondary Growth of CsPbBr₃ Perovskite Nanocrystals

Sumit Kumar Dutta, Narayan Pradhan, et al.

OCTOBER 12, 2021

ACS NANO

READ 🗹

Growth of Perovskite CsPbBr₃ Nanocrystals and Their Formed Superstructures Revealed by In Situ Spectroscopy

He Huang, Bert Nickel, et al.

SEPTEMBER 02, 2020

CHEMISTRY OF MATERIALS

READ 🗹

Get More Suggestions >